Chapter 7

Semidiscrete Finite Element Formulation

As discussed in the introduction to this thesis, finite element methods for the direct solution of transient problems commonly use the technique of semidiscretization in which the spatial domain is discretized using finite elements, producing a system of ordinary differential equations in time which in turn is discretized using finite difference methods. When semidiscrete methods are used for the exterior structural acoustics problem, high-order nonreflecting boundary conditions must be applied to the artificial boundary surrounding the finite computational domain. As shown in Chapters 5 and 6, high-order accurate non-reflecting boundary conditions typically involve high-order temporal derivates in their definitions. As the order of the non-reflecting boundary conditions increases, they become increasingly difficult to implement in a semidiscrete setting due to the occurrence of high-order time derivatives on the truncation boundary. Standard semidiscrete algorithms for second-order hyperbolic equations such as the Newmark family of time integrators are restricted to integrating up to second-order time derivatives, thus when implemented directly, they are limited to second-order accurate boundary conditions $\mathbb{S}_2$. Furthermore, while semidiscrete methods are effective for computing smooth response, their performance is less satisfactory when solving acoustic wave propagation problems exhibiting steep gradients or sharp wave fronts typically arising in the complex radiation and scattering fields found in transient structural acoustics problems. Nevertheless, for transient problems without excessive gradients in the solution, or for time-dependent problems that are driven to steady-state, semidiscrete finite element methods can be an effective technique.

To demonstrate this, we examine the performance of the second-order $\mathbb{S}_2$ non-reflecting boundary condition described in Chapter 6 in a semidiscrete finite element formulation for the coupled structural acoustics problem. The approach is based on the introduction of an artificial boundary Γ_∞ enclosing a computational domain Ω, which is composed of the fluid domain Ω_f which in turn encloses the structural domain Ω_s. The local boundary operators, which are in a form relating Dirichlet to Neumann data, are imposed on the artificial boundary. Finite element semidiscretization of the coupled problem is accomplished using a scalar velocity potential in the fluid domain and displacements in the structure. The resulting system of ordinary differential equations in time is then integrated using a standard finite difference technique. The use of displacement–velocity potential time-dependent global solution vectors $(\boldsymbol{d}, \boldsymbol{\phi})$ for the coupled fluid-structure fields provides a banded and symmetrically coupled system of ordinary differential equations. The use of a scalar potential has the advantage of the *a priori* satisfaction of irrotationality and a reduction in fluid degrees of freedom when compared to vector representations BATHE AND HAHN [1979], BELYTSCHKO [1980b] for the fluid variable. The $(\boldsymbol{d}, \boldsymbol{\phi})$ semidiscrete approach was first introduced by EVERSTINE [1980] to correct the problem resulting from the well-known displacement–pressure $(\boldsymbol{d}, \boldsymbol{p})$ formulation ZIENKIEWICZ AND BETTESS [1978], GLADWELL [1966], and CRAGGS [1971], which results in a non-symmetric system of ordinary equations for the time-dependent case.

7.1 Overview

In Section 7.2, we develop the weak form of the fluid-structure initial boundary-value problem in terms of displacement and velocity potential variables. We also give details on the implementation of second-order non-reflecting boundary conditions in the semidiscrete variational setting. Finite element semidiscrete matrix equations for the coupled system are stated in Section 7.3. Numerical results presented in Section 7.4 illustrate the performance of the two-dimensional time-dependent radiation boundary conditions as affected by frequency, distance from the source of disturbance, and radiation directionality. Accurate results for canonical model problems involving only a single layer of fluid elements have been obtained. Details for the development of consistent fluid-structure coupling elements for the interaction between standard C^0 continuum-based shell elements and acoustic fluid elements are also given in this section. Finally in Section 7.5 conclusions are drawn.

7.2 Coupled Variational Equations

The variational or 'weak' form of the fluid-structure problem corresponding to Eqs. (2.27)–(2.33) may be stated as:

Find $(\boldsymbol{u}\,,\,\phi) \in \mathcal{S} \times \mathcal{T}$, for $t \in [0, T]$ such that $\forall\,(\boldsymbol{w}\,,\,w) \in \mathcal{V} \times \mathcal{W}$,

$$G_s(\boldsymbol{w}\,,\,\boldsymbol{u}) - A(\boldsymbol{w}\,,\,\phi)_{\Gamma_i} = F_s(\boldsymbol{w}) \tag{7.1}$$

$$G_f(w\,,\,\phi) + A(w\,,\,\boldsymbol{u})_{\Gamma_i} = F_f(w) \tag{7.2}$$

where the bilinear operators for the structure and fluid are respectively,

$$G_s(\boldsymbol{w}\,,\,\boldsymbol{u}) := (\boldsymbol{w}, \ddot{\boldsymbol{u}}) + a_s(\boldsymbol{w}, \boldsymbol{u}) \tag{7.3}$$

$$G_f(w\,,\,\phi) := (w, \ddot{\phi}) + a_f(w, \phi) + (w\,,\,\mathbb{S}_m\phi)_{\Gamma_\infty} \tag{7.4}$$

with notation,

$$(\boldsymbol{w}, \ddot{\boldsymbol{u}}) = \int_{\Omega_s} \rho_s\, \boldsymbol{w} \cdot \ddot{\boldsymbol{u}}\; d\Omega \tag{7.5}$$

$$a_s(\boldsymbol{w}, \boldsymbol{u}) = \int_{\Omega_s} \nabla\boldsymbol{w} : \boldsymbol{C} : \nabla\boldsymbol{u}\; d\Omega \tag{7.6}$$

$$a_f(w, \phi) = \int_{\Omega_f} \rho_0\, \nabla w \cdot \nabla\phi\; d\Omega \tag{7.7}$$

$$(w, \ddot{\phi}) = \int_{\Omega_f} \frac{\rho_0}{c^2}\, w\, \ddot{\phi}\; d\Omega \tag{7.8}$$

$$A(\boldsymbol{w}\,,\,\phi)_{\Gamma_i} = \int_{\Gamma_i} \rho_0\, \boldsymbol{w} \cdot \boldsymbol{n}\dot{\phi}\; d\Gamma \tag{7.9}$$

$$A(w\,,\,\boldsymbol{u})_{\Gamma_i} \;=\; \int_{\Gamma_i} \rho_0\; w\; \dot{\boldsymbol{u}} \cdot \boldsymbol{n}\; d\Gamma \tag{7.10}$$

$$F_s(\boldsymbol{w}) \;=\; \int_{\Gamma_\sigma} \boldsymbol{w} \cdot \bar{\boldsymbol{t}}\; d\Gamma \tag{7.11}$$

$$F_f(w) \;=\; \int_{\Omega_f} \rho_0\; w\, f\; d\Omega \tag{7.12}$$

$$(w\,,\,\mathbb{S}_m \phi)_{\Gamma_\infty} \;=\; \int_{\Gamma_\infty} \rho_0\; w\; \mathbb{S}_m\; \phi\; d\Gamma \tag{7.13}$$

and where

$$\mathcal{S} \;=\; \left\{ \boldsymbol{u}(\boldsymbol{x}\,,\,\cdot) | \boldsymbol{u} \in (H^1(\Omega_s))^d \right\} \tag{7.14}$$

$$\mathcal{V} \;=\; \left\{ \boldsymbol{w}(\boldsymbol{x}) | \boldsymbol{w} \in (H^1(\Omega_s))^d \right\} \tag{7.15}$$

The definition of the trial and weighting function spaces $\mathcal{T}$ and $\mathcal{W}$ will in general be dependent on the boundary operator index m. Specific examples will be discussed later. Note that the radiation boundary condition is enforced weakly in (7.13), i.e., it is treated as a natural boundary condition. For example the inner product defined on the truncation boundary by Eq. (7.13) becomes for $m = 1$:

$$(w, \mathbb{S}_1 \phi)_{\Gamma_\infty} = \mathrm{d}_0(w, \phi)_{\Gamma_\infty} + \mathrm{d}_1(w, \dot{\phi})_{\Gamma_\infty} \tag{7.16}$$

where for the first-order operator defined in (6.31) we have,

$$\mathrm{d}_0(w, \phi)_{\Gamma_\infty} \;=\; \int_{\Gamma_\infty} \frac{\rho_0}{2R} w\, \phi\; d\Gamma$$

$$\mathrm{d}_1(w, \dot{\phi})_{\Gamma_\infty} \;=\; \int_{\Gamma_\infty} \frac{\rho_0}{c} w\; \dot{\phi}\; d\Gamma$$

and for $m = 2$:

$$(w, \mathbb{S}_2 \phi)_{\Gamma_\infty} = \mathrm{d}_0(w, \phi) + \mathrm{d}_1(w, \dot{\phi}) + \mathrm{d}_2(w, \ddot{\phi}) \tag{7.17}$$

where for the second-order operator defined in (6.32) we have,

$$\begin{aligned}
\mathrm{d}_0(w,\phi) &= \int_{\Gamma_\infty} \frac{3\rho_0}{8R} w\,\phi\; d\Gamma + \int_{\Gamma_\infty} \frac{\rho_0}{2R} w,_\theta\;\phi,_\theta\; d\Gamma \\
\mathrm{d}_1(w,\dot\phi) &= \int_{\Gamma_\infty} \frac{3\rho_0}{2c} w\,\dot\phi\; d\Gamma + \int_{\Gamma_\infty} \frac{\rho_0 R}{c} w\,\dot\phi,_r\; d\Gamma \\
\mathrm{d}_2(w,\ddot\phi) &= \int_{\Gamma_\infty} \frac{\rho_0 R}{c^2} w\,\ddot\phi\; d\Gamma
\end{aligned}$$

In the above, we have used the identity,

$$\int_{\Gamma_\infty} w\Delta_\Gamma \phi\; d\Gamma = -\int_{\Gamma_\infty} w,_\theta\;\phi,_\theta\; d\Gamma \tag{7.18}$$

which holds over a closed circular boundary.

Note that the boundary operators are local in both space and time, i.e., they are differential operators. As a consequence, when used as boundary conditions on Γ_∞, the resulting semidiscrete finite element equations are a mth order system of ordinary differential equations in time. For orders $m \leq 2$, standard time-stepping schemes such as the Newmark family of algorithms can be used to solve the transient problem directly. However for $m \geq 3$, the boundary operators involve time derivatives up to mth order, which cannot be handled directly with standard time integration schemes, originally designed for second-order problems. To date, the second-order boundary condition is the highest that has been implemented in a semidiscrete finite element formulation; see Pinsky and Abboud [1990,1991a] for the $\mathbb{R}^3$ case and Pinsky,Thompson, and Abboud [1991b,1992] for the $\mathbb{R}^2$ case.

We emphasize that for the boundary conditions $\mathbb{S}_1$ and $\mathbb{S}_2$, the finite element approximations need only be C^0, i.e. the trial and weighting function spaces are defined as:

$$\mathcal{T} = \left\{\phi(\boldsymbol{x},\cdot)|\phi \in H^1(\Omega_f)\right\} \tag{7.19}$$

$$\mathcal{W} = \left\{w(\boldsymbol{x})|w \in H^1(\Omega_f)\right\} \tag{7.20}$$

7.3 Semidiscrete Matrix Equations

The semidiscrete matrix equations are obtained by introducing finite element approximations into the variational equations (7.1) and (7.2). Standard spatial element interpolations for the structure displacements $\boldsymbol{u}$ and fluid velocity potential ϕ are expressed by:

$$\begin{aligned} \boldsymbol{u}^h(\boldsymbol{x},t) &= \boldsymbol{N}^e(\boldsymbol{x})\boldsymbol{d}^e(t) & \in \ \boldsymbol{C}^0(\Omega_s) \\ \phi^h(\boldsymbol{x},t) &= \widetilde{\boldsymbol{N}}^e(\boldsymbol{x})\boldsymbol{\phi}^e(t) & \in \ C^0(\Omega_f) \end{aligned}$$

where $\boldsymbol{N}^e$ and $\widetilde{\boldsymbol{N}}^e$ are the e^{th} element shape functions for the structure and fluid respectively, and $\boldsymbol{d}^e$ and $\boldsymbol{\phi}^e$ are the time-dependent element structure displacement and fluid velocity potential solution vectors. Introducing these approximations into the variational equations (7.1) and (7.2) and enforcing the conditions of the weak form leads to the following semidiscrete matrix problem:

Given $\boldsymbol{f}_s : (0,T) \mapsto \mathbb{R}^{n_{seq}}$, *and* $\boldsymbol{f}_f : (0,T) \mapsto \mathbb{R}^{n_{feq}}$,
Find $\boldsymbol{d} : (0,T) \mapsto \mathbb{R}^{n_{seq}}$ *and* $\boldsymbol{\phi} : (0,T) \mapsto \mathbb{R}^{n_{feq}}$ *such that,*

$$\begin{aligned} &\begin{bmatrix} \boldsymbol{M}_s & \boldsymbol{0} \\ \boldsymbol{0} & -(\boldsymbol{M}_f + \boldsymbol{D}_2) \end{bmatrix} \begin{Bmatrix} \ddot{\boldsymbol{d}} \\ \ddot{\boldsymbol{\phi}} \end{Bmatrix} + \begin{bmatrix} \boldsymbol{D} & \boldsymbol{A} \\ \boldsymbol{A}^T & -\boldsymbol{D}_1 \end{bmatrix} \begin{Bmatrix} \dot{\boldsymbol{d}} \\ \dot{\boldsymbol{\phi}} \end{Bmatrix} \\ &+ \begin{bmatrix} \boldsymbol{K}_s & \boldsymbol{0} \\ \boldsymbol{0} & -(\boldsymbol{K}_f + \boldsymbol{D}_0) \end{bmatrix} \begin{Bmatrix} \boldsymbol{d} \\ \boldsymbol{\phi} \end{Bmatrix} = \begin{Bmatrix} \boldsymbol{f}_s \\ \boldsymbol{f}_f \end{Bmatrix} \end{aligned} \tag{7.21}$$

where $\boldsymbol{d}$ and $\boldsymbol{\phi}$ are the global solution vectors and,

$$\boldsymbol{K}_s = \boldsymbol{K}_s^T = \mathop{\mathsf{A}}_{e=1}^{n_{el}} \int_{\Omega_s^e} (\nabla \boldsymbol{N}^e)^T \,\overline{\boldsymbol{C}}\, (\nabla \boldsymbol{N}^e) \, d\Omega^e \tag{7.22}$$

$$\boldsymbol{M}_s = \boldsymbol{M}_s^T = \mathop{\mathsf{A}}_{e=1}^{n_{el}} \int_{\Omega_s^e} \rho_s \boldsymbol{N}^{eT} \boldsymbol{N}^e \, d\Omega^e \tag{7.23}$$

$$\boldsymbol{K}_f = \boldsymbol{K}_f^T = \mathop{\mathsf{A}}_{e=1}^{n_{el}} \int_{\Omega_f^e} \rho_0 \left(\nabla \widetilde{\boldsymbol{N}}^e\right)^T \left(\nabla \widetilde{\boldsymbol{N}}^e\right) \, d\Omega^e \tag{7.24}$$

$$\boldsymbol{M}_f = \boldsymbol{M}_f^T = \mathop{\mathsf{A}}_{e=1}^{n_{el}} \int_{\Omega_f^e} \frac{\rho_0}{c^2} \widetilde{\boldsymbol{N}}^{eT} \widetilde{\boldsymbol{N}}^e \, d\Omega^e \tag{7.25}$$

$$\boldsymbol{f}_s = \mathop{\mathsf{A}}_{e=1}^{n_{el}} \int_{\Gamma_\sigma^e} \boldsymbol{N}^{eT} \, \bar{\boldsymbol{t}} \, d\Gamma^e \tag{7.26}$$

$$\boldsymbol{f}_f = \mathop{\mathsf{A}}_{e=1}^{n_{el}} \int_{\Omega_f^e} \rho_0 \widetilde{\boldsymbol{N}}^{eT} \, f \, d\Omega^e \tag{7.27}$$

$$\boldsymbol{A} = \mathop{\mathsf{A}}_{e=1}^{n_{el}} \int_{\Gamma_i^e} -\rho_0 \boldsymbol{N}^{eT} \boldsymbol{n} \widetilde{\boldsymbol{N}}^e \, d\Gamma^e \tag{7.28}$$

$$\boldsymbol{D}_0 = \boldsymbol{D}_0^T = \mathop{\mathsf{A}}_{e=1}^{n_{el}} \int_{\Gamma_\infty^e} \rho_0 \left[\frac{H_1(m)}{2r} \widetilde{\boldsymbol{N}}^{eT} \widetilde{\boldsymbol{N}}^e \right. \tag{7.29}$$

$$\left. + \frac{H_2(m)}{2r} \left(\widetilde{\boldsymbol{N}}_{,\theta}^{eT} \widetilde{\boldsymbol{N}}_{,\theta}^e - \frac{1}{4} \widetilde{\boldsymbol{N}}^{eT} \widetilde{\boldsymbol{N}}^e \right) \right] d\Gamma^e \tag{7.30}$$

$$\boldsymbol{D}_1 = \mathop{\mathsf{A}}_{e=1}^{n_{el}} \int_{\Gamma_\infty^e} \frac{\rho_0}{c} (1 + \frac{H_2(m)}{2}) \widetilde{\boldsymbol{N}}^{eT} \widetilde{\boldsymbol{N}}^e \, d\Gamma^e \tag{7.31}$$

$$+ \int_{\Gamma_\infty^e} \frac{\rho_0 r}{c} H_2(m) \widetilde{\boldsymbol{N}}^{eT} \widetilde{\boldsymbol{N}}_{,r}^e \, d\Gamma^e \tag{7.32}$$

$$\boldsymbol{D}_2 = \boldsymbol{D}_2^T = \mathop{\mathsf{A}}_{e=1}^{n_{el}} \int_{\Gamma_\infty^e} \frac{\rho_0 r}{c^2} H_2(m) \widetilde{\boldsymbol{N}}^{eT} \widetilde{\boldsymbol{N}}^e \, d\Gamma^e \tag{7.33}$$

where n_{el} is the number of elements, $\mathop{\mathsf{A}}_{e=1}^{n_{el}}$ denotes the element assembly operator and $H_i(m)$ is a discrete Heavyside function defined such that $H_i(m) = 1$ if m is greater than or equal to i, and zero otherwise. $\boldsymbol{K}_s$ and $\boldsymbol{M}_s$ are the symmetric stiffness and mass matrices respectively for the structure while $\boldsymbol{K}_f$ and $\boldsymbol{M}_s$ are the corresponding stiffness and mass matrices for the acoustic fluid. $\overline{\boldsymbol{C}}$ is the symmetric constitutive matrix for the structure and $\boldsymbol{D}$ is a symmetric structural damping matrix. Fluid-structure interface elements enforce the coupling between the fluid and structure through the $\boldsymbol{A}$ matrix. $\boldsymbol{D}_0$, $\boldsymbol{D}_1$, and $\boldsymbol{D}_2$ are the matrix contributions arising from the non-reflecting boundary conditions. The resulting system of differential equations is symmetric and banded except for the nonsymmetric element matrix contribution $\boldsymbol{D}_1$ arising from the nonsymmetric boundary integral term in d_1 for $m = 2$. Boundary conditions of order $m \geq 3$ have not been implemented. These boundary conditions would lead to the necessity of increased continuity between elements and semidiscrete matrix equations that will include time derivatives up to order m.

Remark

- The displacement–velocity potential $(\boldsymbol{d}, \boldsymbol{\phi})$ system above can easily be reformulated into the well-known displacement–pressure $(\boldsymbol{d}, \boldsymbol{p})$ approach. The velocity potential is eliminated in favor of the pressure by substituting the discrete momentum balance relation $\boldsymbol{p} = -\rho_0 \dot{\boldsymbol{\phi}}$ into the lower partition of (7.21), multiplying through by ρ_0 and differentiating in time. The resulting $(\boldsymbol{d}, \boldsymbol{p})$ matrix problem becomes,

$$\begin{bmatrix} \boldsymbol{M}_s & \boldsymbol{0} \\ \rho_0 \boldsymbol{A}^T & (\boldsymbol{M}_f + \boldsymbol{D}_2) \end{bmatrix} \begin{Bmatrix} \ddot{\boldsymbol{d}} \\ \ddot{\boldsymbol{p}} \end{Bmatrix} + \begin{bmatrix} \boldsymbol{D} & \boldsymbol{0} \\ \boldsymbol{0} & \boldsymbol{D}_1 \end{bmatrix} \begin{Bmatrix} \dot{\boldsymbol{d}} \\ \dot{\boldsymbol{p}} \end{Bmatrix}$$

$$+ \begin{bmatrix} \boldsymbol{K}_s & -\frac{1}{\rho_0}\boldsymbol{A} \\ \boldsymbol{0} & (\boldsymbol{K}_f + \boldsymbol{D}_0) \end{bmatrix} \begin{Bmatrix} \boldsymbol{d} \\ \boldsymbol{p} \end{Bmatrix} = \begin{Bmatrix} \boldsymbol{f}_s \\ \boldsymbol{f}_f \end{Bmatrix} \tag{7.34}$$

  The effect of this reformulation is to move the coupling matrices, $\boldsymbol{A}$, from the extended damping matrix to the extended mass and stiffness matrices. The principle disadvantage of this pressure formulation is the nonsymmetric system of equations that result.

7.3.1 A consistent fluid-structure coupling element

In this section a consistent fluid-structure coupling element is developed for the interaction between standard C^0 continuum-based shell elements and the acoustic elements. Fluid-structure interface finite elements generate the consistent coupling matrix defined by (7.28). These elements serve as a transition between the structure and fluid, having both structural and fluid nodes. The coupling matrix is restated as,

$$\boldsymbol{A} = \mathop{\mathbf{A}}_{e=1}^{n_{el}} (\boldsymbol{A}^e), \qquad \boldsymbol{A}^e = [\boldsymbol{A}^e_{ab}] = \int_{\Gamma^e_i} -\rho_0 \boldsymbol{N}^{eT}_a \boldsymbol{n} \widetilde{\boldsymbol{N}}^e_b \, d\Gamma^e \tag{7.35}$$

In the above and subsequent equations the index a takes values of 1 to n_{esn}, the number of element structural nodes, and b takes values of 1 to n_{efn}, the number of fluid nodes. The total number of nodes per interface element, n_{en}, is the sum of n_{esn} and n_{efn}. Both structural and fluid nodes lie on the interface boundary Γ_i^e.

Specializing to shell kinematics, the displacement vector $\boldsymbol{u}$ is parameterized by the element natural coordinates $(\xi, \eta, \zeta) \in (-1,1)^3$ and has the following form:

$$\boldsymbol{u}(\xi, \eta, \zeta) = \sum_{a=1}^{n_{esn}} N_a(\xi, \eta) \bar{\boldsymbol{u}}_a + \zeta \sum_{a=1}^{n_{esn}} N_a(\xi, \eta) \frac{t_a}{2} \hat{\boldsymbol{u}}_a \tag{7.36}$$

where $\bar{\boldsymbol{u}}_a$ is the displacement of the element reference surface, $\hat{\boldsymbol{u}}_a$ is the displacement due to the rotation of the shell cross section, and t_a is the thickness at each node. $N_a(\xi, \eta)$ denotes a two-dimensional shape function associated with node a. The vector $\hat{\boldsymbol{u}}_a$ is constructed such that the cross sectional fiber may rotate, but not stretch, viz.,

$$\hat{\boldsymbol{u}}_a = \theta_{a2} \boldsymbol{e}_{a1}^f - \theta_{a1} \boldsymbol{e}_{a2}^f \tag{7.37}$$

The angles θ_{a1} and θ_{a2} represent the rotations of the fiber about the orthonormal basis vectors $\boldsymbol{e}_{a1}^f$ and $\boldsymbol{e}_{a2}^f$, respectively. Further details of the shell kinematics can be found in Hughes [1987].

An expression for the nodal structural shape function matrix is obtained as,

$$\boldsymbol{u} = \sum_{a=1}^{n_{esn}} \boldsymbol{N}_a \boldsymbol{d}_a \ , \quad \boldsymbol{N}_a = N_a \begin{bmatrix} 1 & 0 & 0 & -z_a e_{a12}^f & z_a e_{a11}^f \\ 0 & 1 & 0 & -z_a e_{a22}^f & z_a e_{a21}^f \\ 0 & 0 & 1 & -z_a e_{a32}^f & z_a e_{a31}^f \end{bmatrix} , \quad \boldsymbol{d}_a = \begin{Bmatrix} \bar{\boldsymbol{u}}_a \\ \theta_{a1} \\ \theta_{a2} \end{Bmatrix} \tag{7.38}$$

where $z_a = \zeta t_a / 2$. The fluid nodes have only one velocity potential degree of freedom per node and are interpolated using standard shape functions:

$$\phi = \sum_{b=1}^{n_{efn}} \widetilde{N}_b(\xi, \eta) \phi_b \tag{7.39}$$

Substitution of the shape functions for the shell nodes, $\boldsymbol{N}_a$, and fluid nodes, $\widetilde{N}_b$, into (7.35) results in,

$$\boldsymbol{A}_{ab}^e = \int_{\Gamma_i^e} -\rho_0 N_a \widetilde{N}_b \begin{bmatrix} \boldsymbol{n} \\ -z_a \boldsymbol{e}_{a2}^f \cdot \boldsymbol{n} \\ z_a \boldsymbol{e}_{a1}^f \cdot \boldsymbol{n} \end{bmatrix} d\Gamma^e, \qquad \boldsymbol{n} = \frac{\boldsymbol{e}_\xi \times \boldsymbol{e}_\eta}{\|\boldsymbol{e}_\xi \times \boldsymbol{e}_\eta\|} \tag{7.40}$$

where $\zeta = 1$ at the interface boundary Γ_i^e, $\boldsymbol{n}$ is the unit normal outward from the interface boundary, and $\boldsymbol{e}_\xi$ and $\boldsymbol{e}_\eta$ are unit tangent vectors in the ξ- and η- coordinate directions respectively. Note that different orders of interpolation for the structural nodes vs. the fluid nodes can be accommodated, allowing possible combinations such as quadratic interpolation for shell nodes and cubic interpolation for fluid nodes.

7.4 Numerical Examples

In this section numerical studies are performed to assess the accuracy of the local non-reflecting boundary conditions implemented in a semidiscrete finite element formulation, as effected by the operator order, acoustic wave number, radiation directionality, and distance from the acoustic source. In all the results to follow, the semidiscrete matrix equations are integrated in time using the standard second-order accurate trapezoidal rule. Numerical results are obtained using the simple 'plane-wave' (PW) damper and the first two local boundary operators defined in (6.31) and (6.32), and implemented in (7.16) and (7.17). In the following discussions, the notation for the local operators $\mathbb{S}_1$ and $\mathbb{S}_2$ will be replaced with the notation B_1-damper and B_2-damper to distinguish the semidiscrete implementation of these operators.

7.4.1 Uniform acoustic radiation

Consider the uncoupled problem of an infinite cylindrical radiator of radius $a = 1$, pulsating uniformly with a Dirichlet boundary condition $\phi(a,t) = \phi_o sin\omega t$ for $t > 0$ on the wet surface. The steady-state solution is a circular cylindrical wave given by (6.5) where R is replaced by a, and $n = 0$.

$$\phi(r,t) = -\mathrm{Imag}\left\{\frac{H_0(kr)}{H_0(ka)}\,\phi_o\,e^{-i\omega t}\right\} \qquad \text{for } r \in [a, +\infty] \tag{7.41}$$

A series of transient finite element solutions were obtained for this problem using zero initial conditions on ϕ and $\dot{\phi}$ and a time increment of $\Delta t = 0.2$. The nondimensional wavenumber is set at $ka = 1$. The artificial boundary is positioned at $R = 6a$ and then reduced to $R = 1.5a$ in order to examine the influence of radial distance on the accuracy of the non-reflecting boundary conditions. Discretization in the radial direction was kept constant with an element dimension of $h^e = 0.5$ in this direction, corresponding to 4π elements per wavelength. Bilinear elements are used throughout and the following definitions employed; Mesh L1: $n = 1$, $R = 1.5$ and Mesh L2: $n = 10$, $R = 6.0$.

Figure 7.1 shows the profiles of the exact and transient finite element solutions in the fluid along a ray at two sample times. The solution sample times are such that many spurious reflections between the truncation boundary and cylinder could have occurred. In Figure 7.1a, results for $R = 6$ and 10 elements in the radial direction indicate that the as expected the B_1 operator is nearly exact. The plane-wave damper (PW) performs well at this value of R. Figure 7.1b shows results for $R = 1.5$ with a single element in the radial direction. The operator B_1 remains accurate whereas the solution accuracy for the plane-wave damper deteriorates significantly. This observation is clear from the time-dependent solution measured on the artificial boundary $r = R$, see Figure 7.2.

7.4.2 Fluid-structure interaction example

Now consider the coupled problem of an elastic infinite cylindrical thin shell submerged in an acoustic fluid, subject to time-harmonic uniform internal pressure loading,

$$p = p_o e^{-i\omega t} \tag{7.42}$$

The governing equation for a cylindrical shell of radius a, submerged in the fluid under plane-strain conditions is

$$(k_s - \omega^2 m_s) u_r = p_o - i\omega\rho_o\phi(a) \tag{7.43}$$

where u_r is the radial displacement of the shell, p_o is the applied pressure, the last term on the right hand side represents fluid pressure loading, and k_s and m_s are the shell stiffness and mass per unit area, respectively, given by:

$$k_s = \frac{Eh}{a^2(1-\nu^2)}, \qquad m_s = \rho_s h \tag{7.44}$$

In the above, E and ν are the Young's modulus and Poisson's ratio for the shell material, h is the thickness and ρ_s is the shell density.

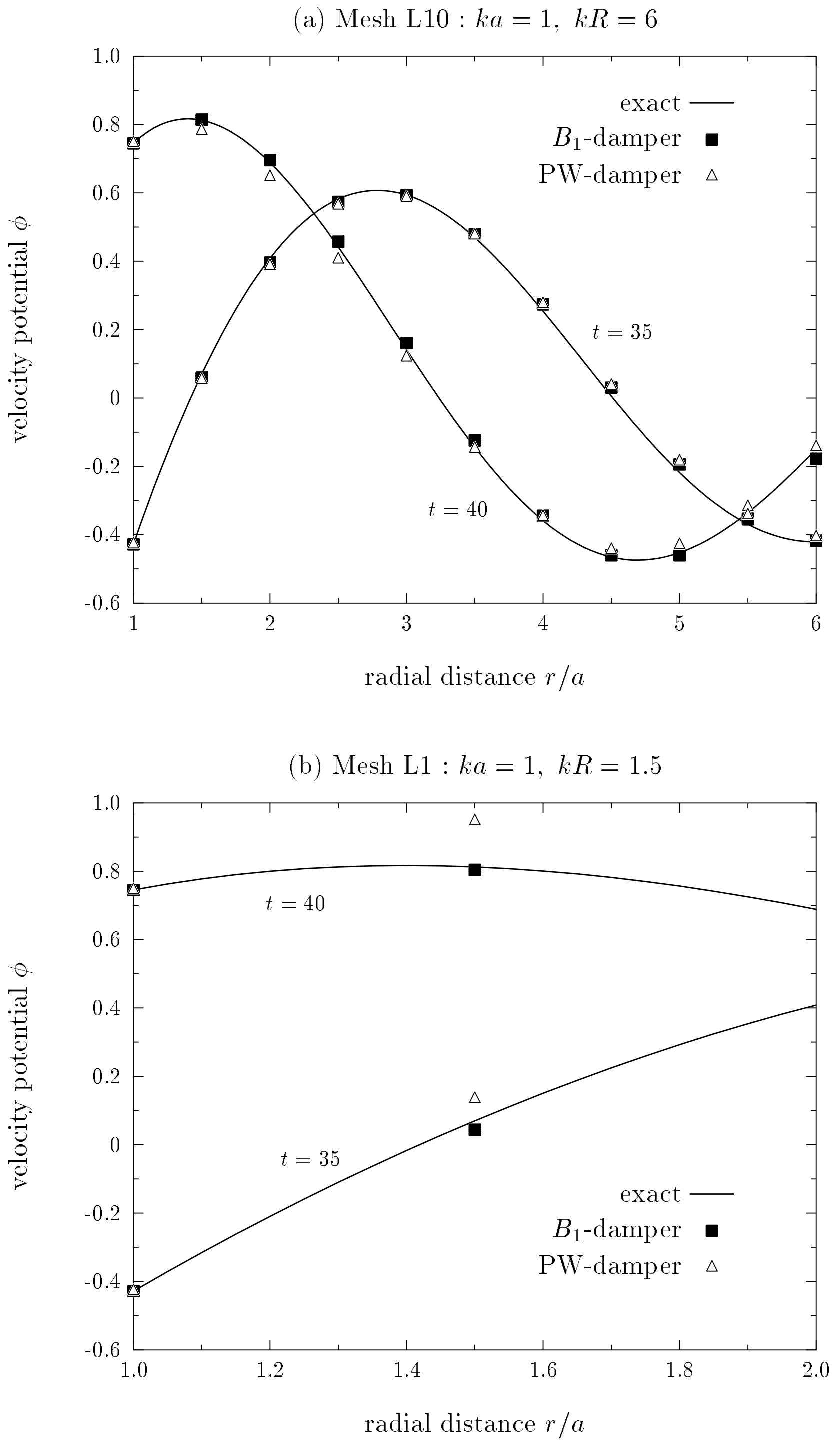

Figure 7.1: Uniformly pulsating cylindrical radiator. Solution profile at time $t = 35$ and $t = 40$: (a) $kR = 6$ (b) $kR = 1.5$.

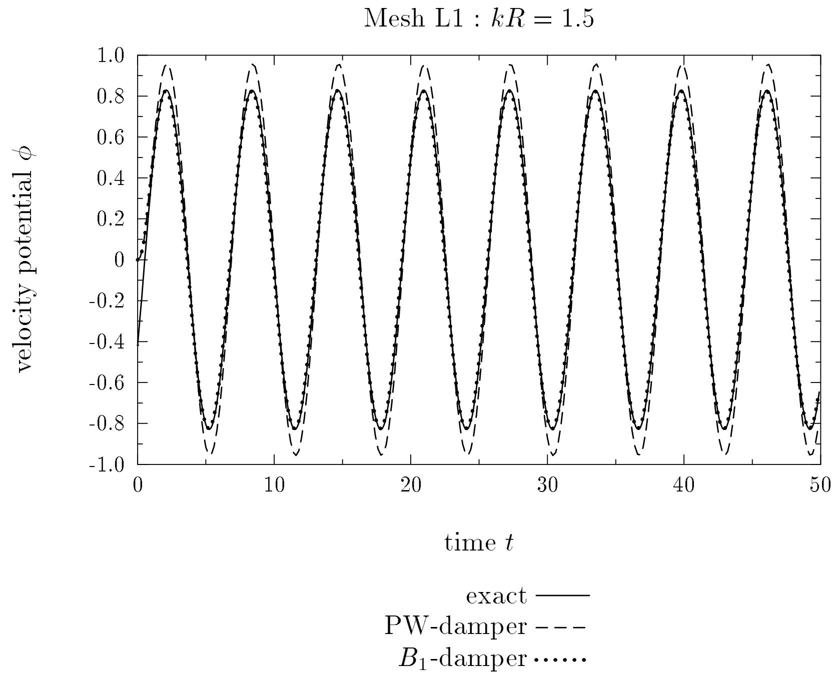

Figure 7.2: Uniformly pulsating cylindrical radiator. Solution at $r = R$.

The exact solution for the velocity potential and shell radial displacement is,

$$\phi(r,t) = ic\frac{H_0(kr)}{H_1(ka)}u_r(t) \tag{7.45}$$

$$u_r(t) = \frac{p_o e^{-i\omega t}}{\left(k_s - \omega^2 m_s - \omega\rho_o c\dfrac{H_0(ka)}{H_1(ka)}\right)} \tag{7.46}$$

A finite element solution of this problem was obtained using the following values. The shell has a radius of $a = 1.0$ and thickness $h = 1/20$. The material properties of the shell are $E = 91. \times 10^6$, $\nu = 0.3$, and $\rho_s = 1000$. The fluid properties are the same as those considered in the previous case with $c = 1.0$ and $\rho_o = 2.0$. The structure is modeled using standard C^0 linear continuum–based shell elements with transverse shear capability. Bilinear Lagrange based shell elements with selectively reduced integration were employed with plane-strain boundary conditions. The consistent fluid-structure coupling element developed earlier in Section 7.3.1 is used to couple the shell to the acoustic fluid elements. Details of the shell formulation can be found in HUGHES [1987]. The fluid discretization is identical to that used previously in the uncoupled case.

The numerical solution obtained using a truncation radius of $R = 6$ and 10 acoustic elements in the radial direction was extremely accurate for all three boundary conditions tested. In this case the exact and numerical solutions were nearly coincident (not shown). Fig. 7.3 compares the analytical solution for radial displacement and the acoustic fluid velocity potential with the finite element solution when the radius to the truncation boundary is reduced to $R = 1.5$ with only a single fluid element in the radial direction. The results are displayed for a point on the fluid-shell interface Γ_i, i.e. at $a = 1$. The operator B_1 is very accurate and performs better than the B_2 and PW operators for this uniform wave problem.

Now consider the same infinite elastic cylindrical shell submerged in an acoustic fluid, subject to a step in internal pressure, $p(a,t) = p_o$ for $t > 0$ and zero initial conditions. The shell properties are the same as those in the previous example except that the Young's modulus is changed to $E = 910.$, such that the shell breathing mode characteristic frequency in vacuum is $\omega_o = \sqrt{k_s/m_s} = 1$ (this choice accentuates the transient character of the solution). The fluid properties are the same as those used previously.

Since an exact solution for this problem is not readily obtainable, we take as a basis for comparison, a numerical solution obtained using an extensive and fine mesh of acoustic elements with a truncation radius of $R = 26$ (this solution is labeled 'infinite mesh' in Figures 7.4 and 7.5). This mesh is large enough that the wave front will not reach the truncation boundary of the computational fluid domain during the analysis time span.

Figure 7.4 shows the solution time history for the structure radial displacement and fluid velocity potential at the structure-fluid interface for the mesh with $R = 6$ having 10 elements in the radial direction. Figure 7.5 shows the results for these solutions obtained with the mesh with $R = 1.5$ and one fluid element in the radial direction. For both meshes, the structure radial displacement is computed accurately for both B_1 and B_2 conditions, Figures 7.4a and 7.5a. Solutions with the PW damper are somewhat inferior at $R = 1.5$.

Figures 7.4b and 7.5b show comparisons of the velocity potential ϕ at the fluid–structure interface as the truncation boundary Γ_∞ is brought closer to the structure.

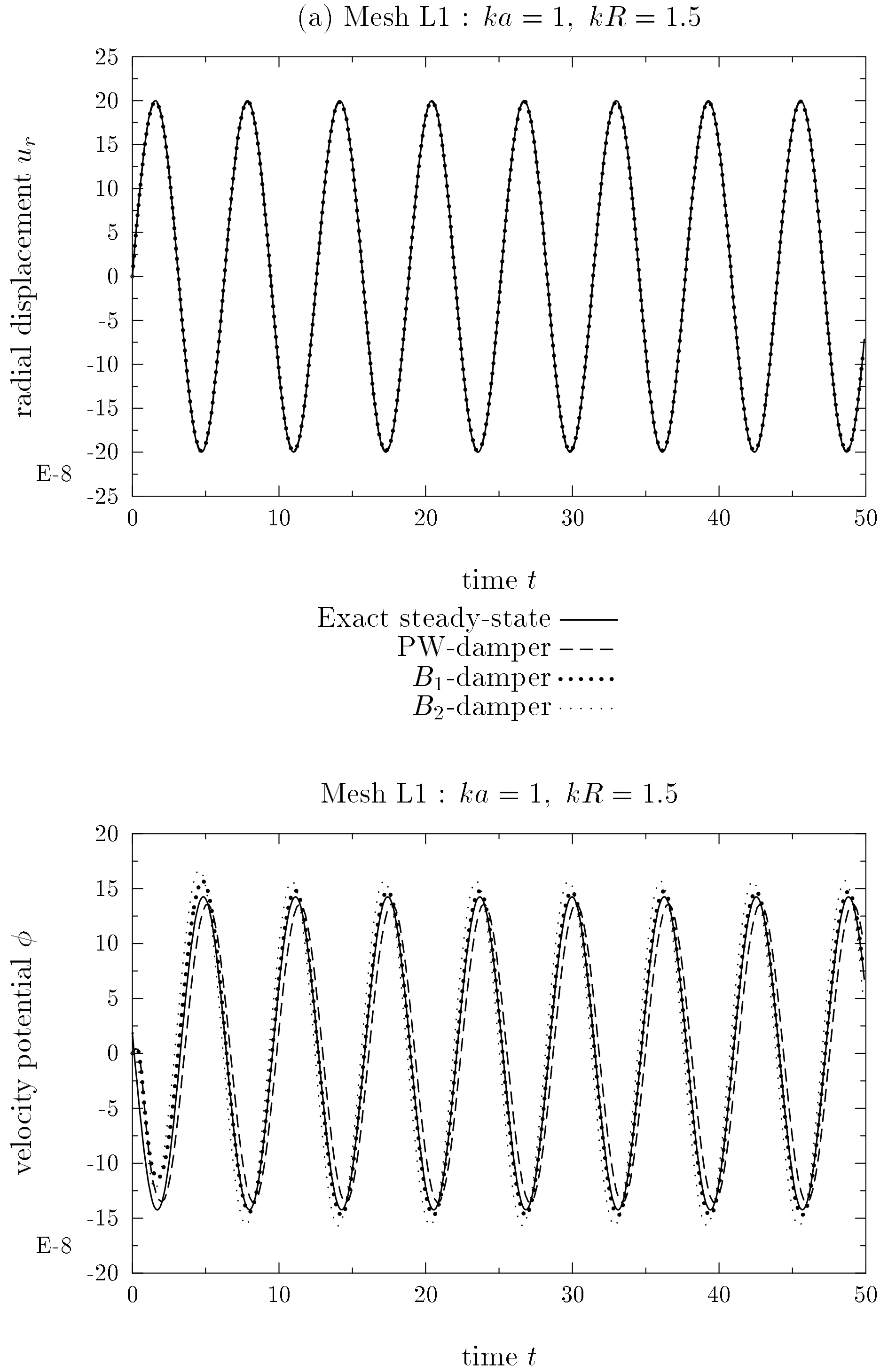

Figure 7.3: Submerged elastic cylinder subject to sinusoidal internal pressure. Solution at the fluid-shell interface for $kR = 1.5$.

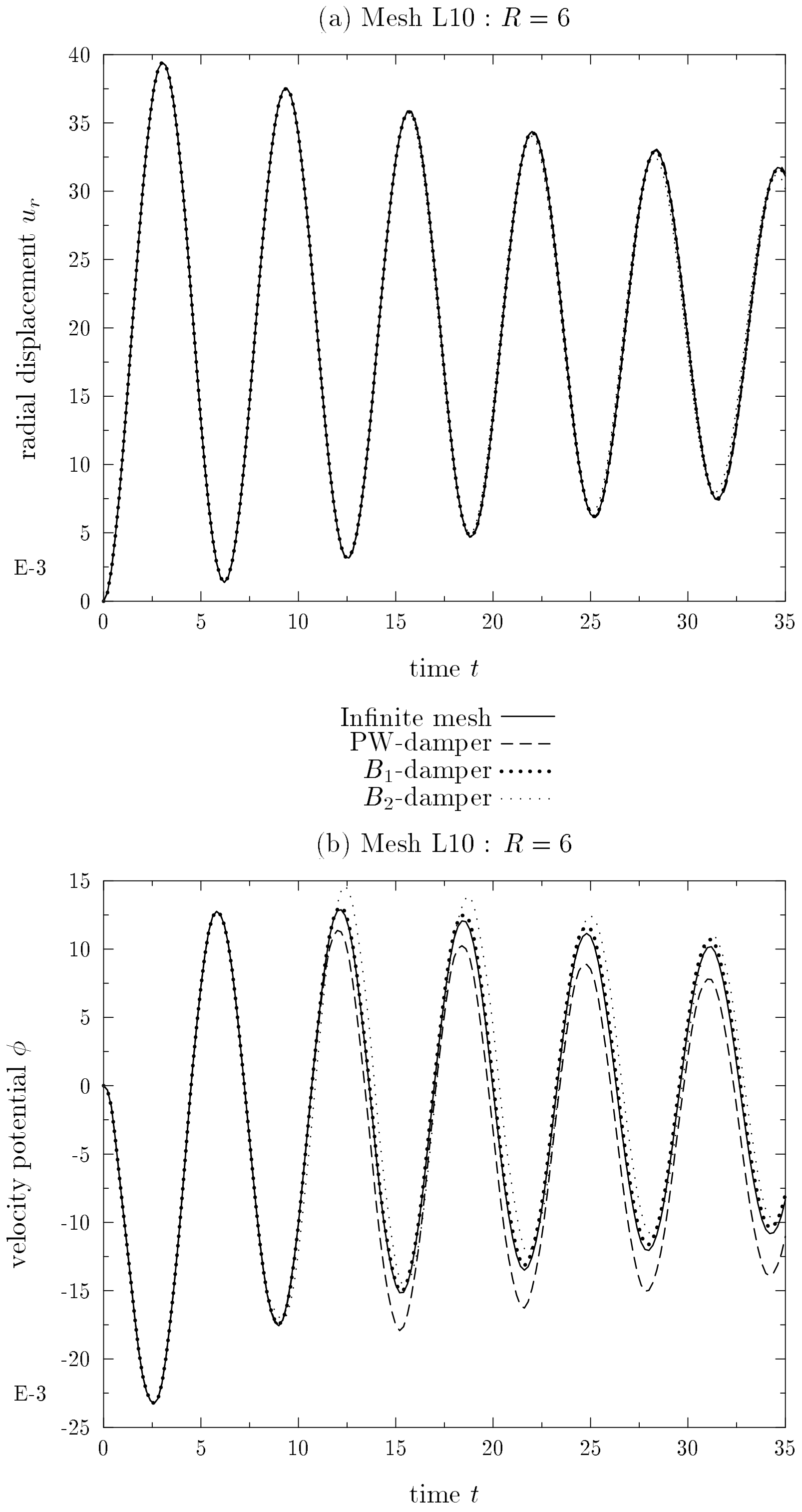

Figure 7.4: Submerged elastic cylinder subject to step in internal pressure. Solution at the fluid-shell interface for $R = 6$. (a) Shell radial displacements.(b) Acoustic fluid velocity potential.

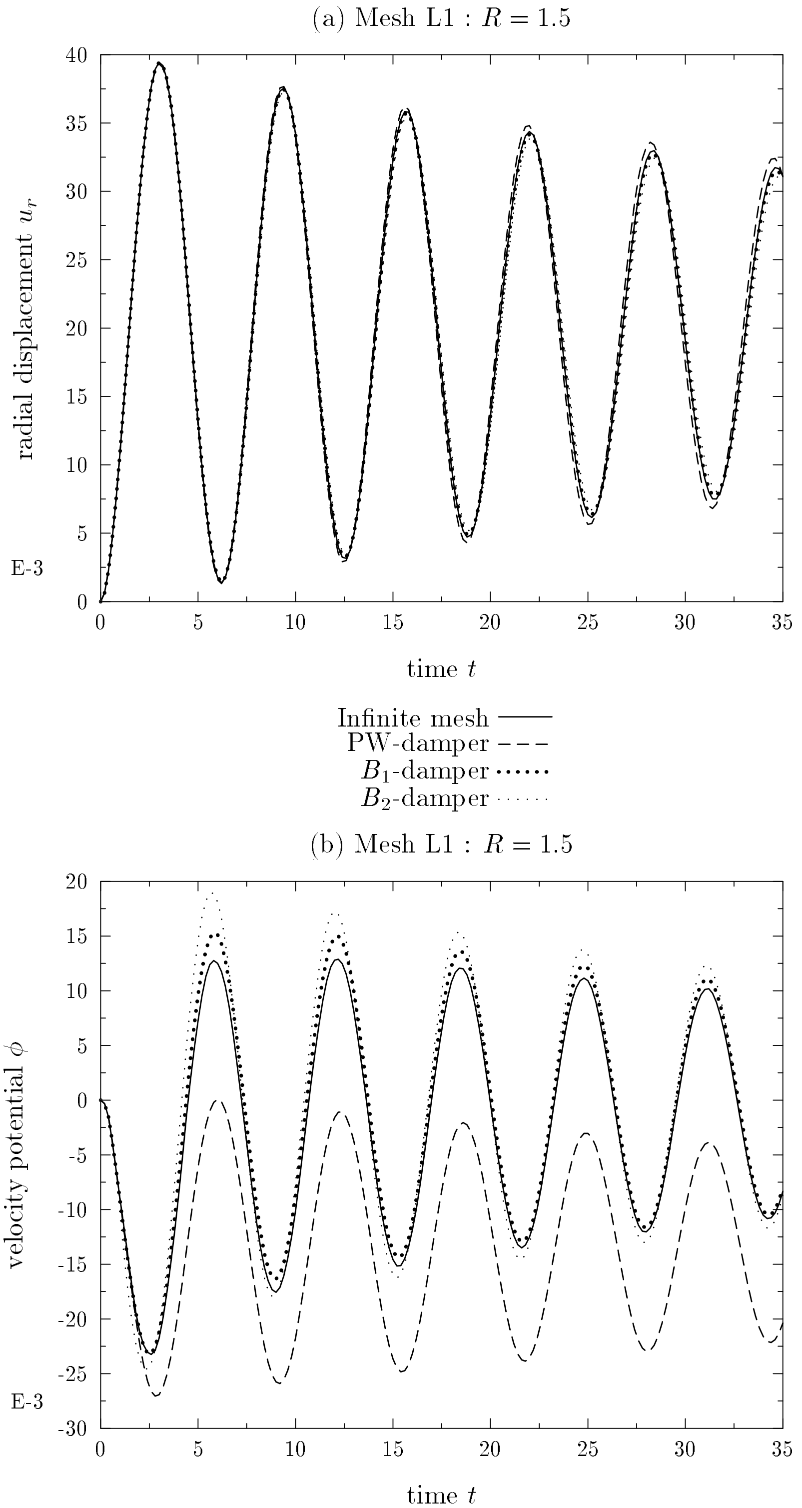

Figure 7.5: Submerged elastic cylinder subject to step in internal pressure. Solution at the fluid-shell interface for $R = 1.5$. (a) Shell radial displacements.(b) Acoustic fluid velocity potential.

It is observed that the transient response is captured accurately by the B_1 operator while the B_2 solution displays some error in the early-time but quickly converges to the coupled fluid-shell breathing mode response predicted by the infinite/finite element mesh solution. The PW damper results exhibit significant spurious reflections as indicated by severe amplitude and phase errors. These results demonstrate that for the simple case of uniform radiation, the B_1 operator performs optimally.

7.4.3 Nonuniform acoustic radiation

It is expected that as the radiation pattern becomes more complex, the higher order operators B_m will be increasingly accurate when compared to the simple PW damper. To investigate the performance of the dampers in transmitting non-uniform acoustic radiation when implemented in a semidiscrete finite element method, the problem of an infinite circular cylindrical radiator with circumferentially harmonic loading $\phi(a,\theta,t) = \phi_o \cos n\theta \sin \omega t$ for $t > 0$ is solved with a time step of $\Delta t = 0.2$ and zero initial conditions. The finite element calculations were based on a uniform fluid mesh of quadratic elements, denoted Mesh Q5, with 5 elements in the radial direction and 10 elements in the circumferential direction (100 elements).

Figure 7.6 shows the solution profile around the artificial boundary as the circumferential mode n ranges from 1 through 5, and $ka = 4$. It is observed that as n is increased, the B_2 operator is able to accurately capture the non-uniform wavefronts in the higher circumferential modes, while the lower order boundary conditions begin to lose accuracy in the higher spatial harmonics, Figure 7.6b. In a second calculation we reduce the nondimensional wavenumber to $ka = 1$. The results for the first three modes are shown in Figure 7.7. In this case, the B_2 condition is clearly superior to the other conditions tested. These numerical results support our earlier conclusions: as we increase the order m of the operator B_m, we increase the order of accuracy and are able to capture progressively more complex radiation patterns.

In Chapter 6 it was noted that for a fixed order m and radius R, as the acoustic wavenumber k is increased, the accuracy of B_m is increased, i.e. $\lim_{k\to\infty} B_m(\phi) = 0$. To examine the effect of increasing wavenumber consider the non-uniform radiation from a cylinder with constant time-harmonic velocity potential $\phi(a,\theta,t) = \phi_o \sin(\omega t)$, prescribed on the arc, $(-\theta_o \leq \theta \leq \theta_o)$. Elsewhere on the wet surface, $\phi(a,\theta,t) = 0$.

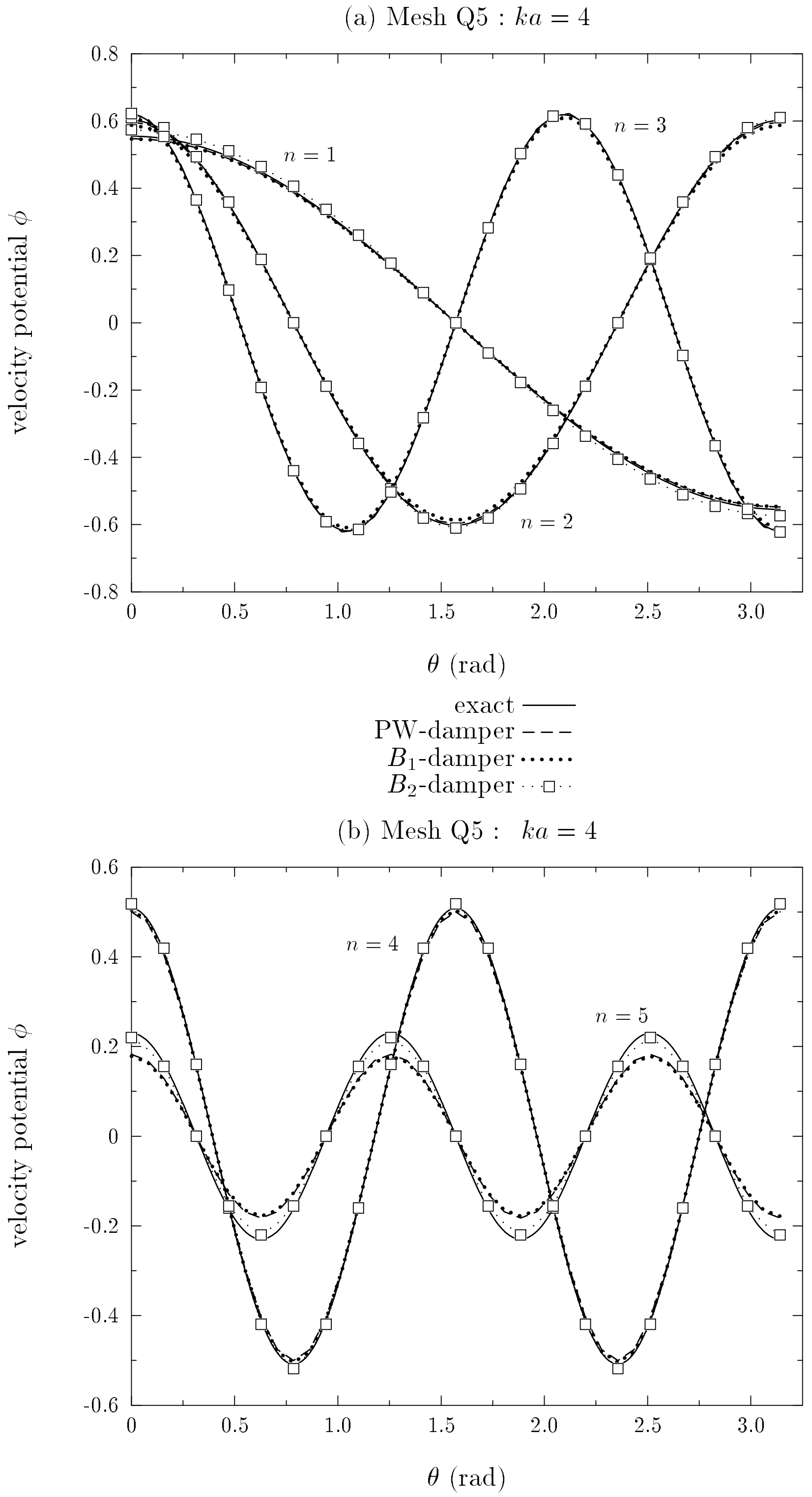

Figure 7.6: Radiating rigid cylinder with $\cos n\theta$ circumferential harmonics of order n, for $ka = 4$. Solution profile on the radiation boundary at time $t = 30$: (a) $n = 1, 2, 3$ (b) $n = 4, 5$.

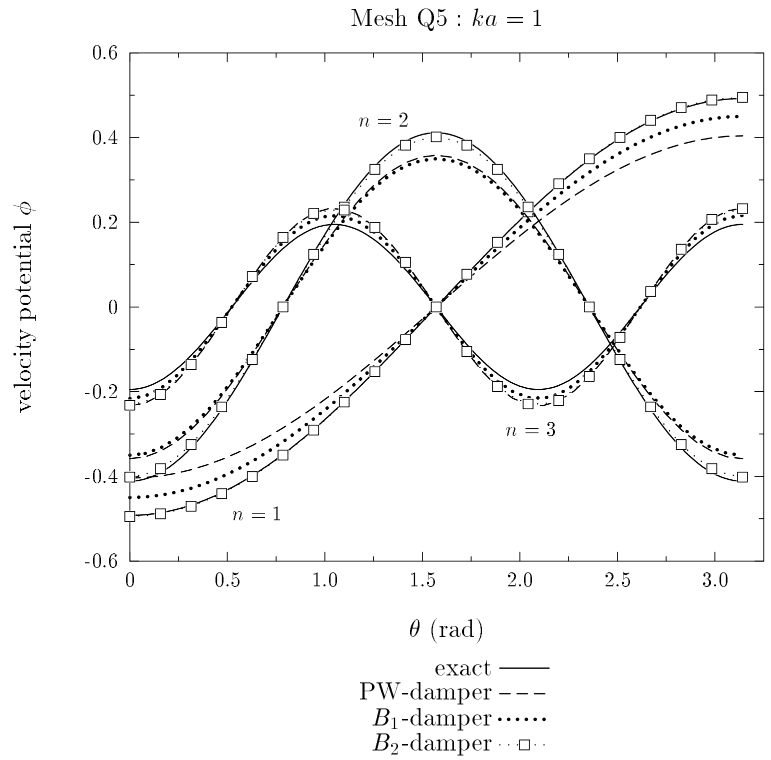

Figure 7.7: Radiating rigid cylinder with $\cos n\theta$ circumferential harmonics of order n, for $ka = 1$. Solution profile on the radiation boundary at time $t = 30$ with $n = 1, 2, 3$.

The problem is solved numerically as a transient semidiscrete problem where the wavenumber is increased from $ka = 1$ through $ka = 6$. The solution profile around the circumference of the radiation boundary is depicted in Figure 7.8 at fixed time $t = 40$. The exact solution is accurately captured by all the dampers throughout the domain for $ka \geq 3$. Note that in the vicinity of the source ($0 \leq \theta \leq \theta_o$), the solution is dominated by the 'breathing' mode defined by $n = 0$. In this region, the B_1-damper is the most accurate. As the backside is approached, the amplitude has been attenuated down to a few percent of the source position and the B_2-damper is the most accurate. Below $ka = 3$, the PW and B_1 dampers begin to lose accuracy, yet the B_2 damper is able to maintain accuracy down to $ka = 1$.

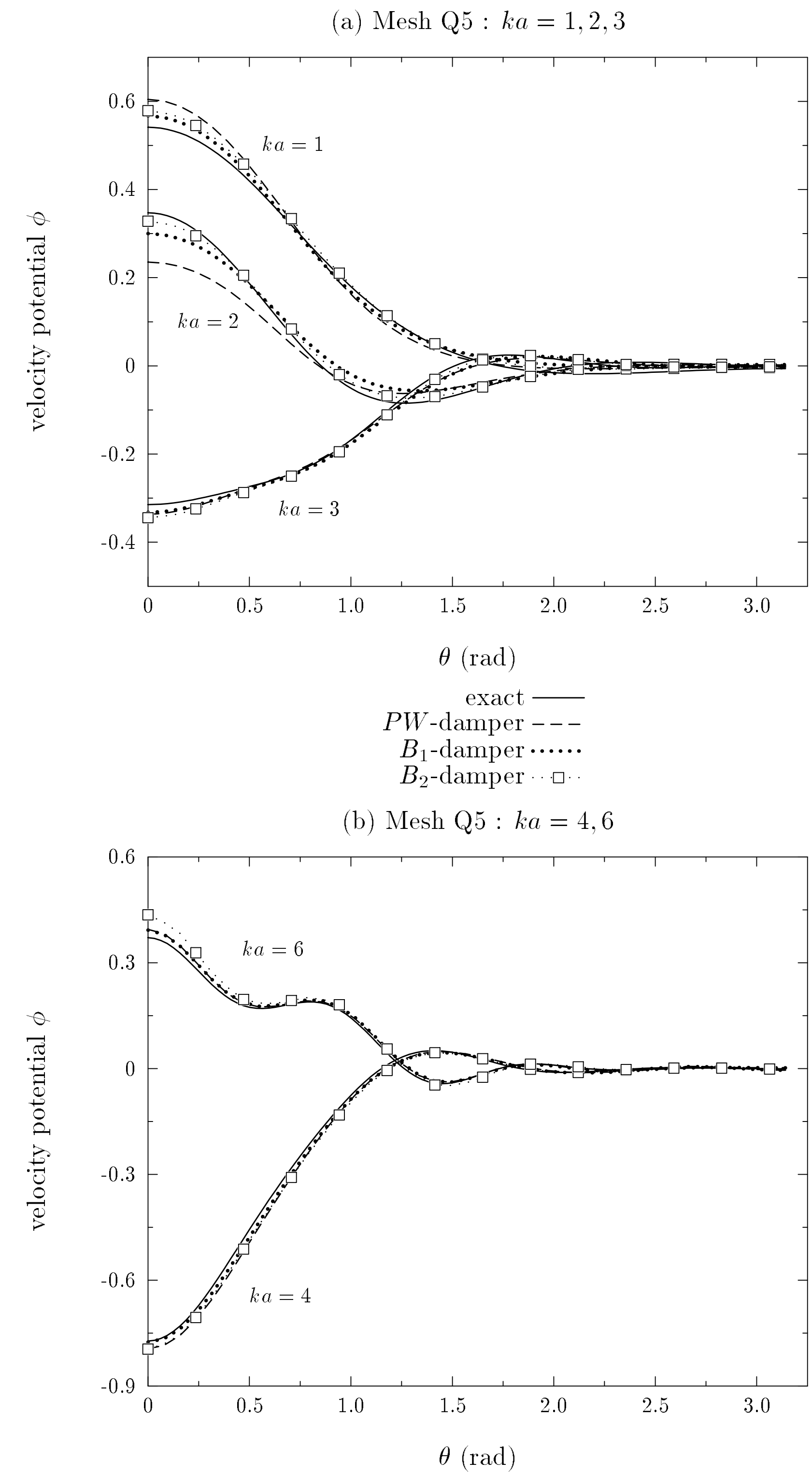

Figure 7.8: Radiation from an element of a cylinder. Solution profile on the radiation boundary at time $t = 40$. (a) $ka = 1, 2, 3$ (b) $ka = 4, 6$.

7.5 Summary and Conclusions

In this chapter the sequence of local radiation boundary operators described in Chapter 6 have been incorporated into a general coupled semidiscrete finite element formulation for transient analysis. Consistent fluid-structure coupling elements are developed for the interaction between standard C^0 continuum-based shell elements and acoustic fluid elements. It has been shown that the local boundary conditions preserve the data structure of the standard finite element method and up to order $m = 2$ are easily incorporated into semidiscrete finite element programs. Boundary conditions of order $m \geq 3$ have not been implemented. These boundary conditions would lead to the necessity of increased continuity between elements and semidiscrete matrix equations that must include time derivatives up to order m. The design of stable time integration algorithms capable of incorporating third order and higher boundary conditions remains an open question. It is this limitation of the semidiscrete approach that motivated the development of the space-time finite element approach for the exterior structural acoustics problem, where their is no intrinsic restriction on the order of time derivative appearing in the governing equations.

Numerical results comparing the performance of the first- and second- order local absorbing boundary conditions in a semidiscrete approach confirm the superiority of B_2 over B_1. Accurate results have been obtained with the B_2 operator using only a single layer of acoustic fluid elements. In the case of uniform radiation, we note for the B_2 operator a slight decrease in accuracy compared to the B_1 operator, which we have shown performs optimally for this case. However, for non-uniform acoustic radiation involving higher order wave harmonics, results indicate that the B_2 condition outperforms the lower-order conditions as expected. Further numerical examples for the semidiscrete approach can be found in ABBOUD [1990], PINSKY AND ABBOUD [1990,1991a] for three-dimensional problems and PINSKY, THOMPSON, AND ABBOUD [1991b,1992] for two-dimensional problems.